

An Approximate Solver for Riemann and Riemann-like Ellipsoidal Configurations

Shangli Ou

*Department of Physics & Astronomy and Center for Computation & Technology,
Louisiana State University, Baton Rouge, LA 70803*

ABSTRACT

We introduce a new technique for constructing three-dimensional (3D) models of incompressible Riemann S-type ellipsoids and compressible triaxial configurations that share the same velocity field as that of Riemann S-type ellipsoids. Our incompressible models are exact steady-state configurations; our compressible models represent approximate steady-state equilibrium configurations. Models built from this method can be used to study a variety of relevant astrophysical and geophysical problems.

Subject headings: Riemann S-type ellipsoids— 3D self-consistent-field methods — — equilibrium configurations — computational astrophysics

1. Introduction

Our understanding of stellar structure and stability has been built upon classical analytical studies of equilibrium configurations of incompressible self-gravitating systems by Maclaurin, Jacobi, Dedekind, Darwin, Riemann, and especially Chandrasekhar (1969). With the help of modern computers and numerical methods, such as the self-consistent-field (SCF) technique (Ostriker & Mark 1968; Hachisu 1986a) and hydrodynamics techniques, these studies have been extended to compressible configurations by a variety of researchers (Tohline, Durisen, & McCollough 1985; Hachisu 1986a,b; Williams & Tohline 1988; Cazes & Tohline 2000; Shibata, Karino, & Eriguchi 2002). However, most three-dimensional (3D) hydrodynamical studies have been confined to a limited parameter space, i.e., starting from two-dimensional (2D) axisymmetric equilibrium models (compressible analogues of Maclaurin spheroids) because we have not been able to build 3D compressible equilibrium models with complicated flows. To the author's knowledge, techniques have only been developed to build compressible equilibrium models of nonaxisymmetric configurations for a few systems with simplified rotational profiles, e.g., rigidly rotating systems (Hachisu & Eriguchi 1984; Hachisu

1986b), irrotational systems (Uryu & Eriguchi 1998), and configurations that are stationary in the inertial frame (Uryu & Eriguchi 1996). Our aim is to find a method by which a much wider class of nonaxisymmetric configurations can be readily constructed. This will permit us to more clearly understand the viability of evolutionary sequences of triaxial configurations and will provide models whose stability properties can be readily analyzed.

Previous linear stability analyses (Chandrasekhar 1969; Lifschitz & Lebovitz 1993; Lebovitz & Lifschitz 1996; Lebovitz & Saldanha 1999) have revealed a number of hydrodynamical instabilities that might arise in incompressible Riemann ellipsoids, but no corresponding numerical work using state-of-the-art 3D hydrodynamic techniques has been carried out. In particular, Riemann S-type ellipsoids have been found to be subject to a hydrodynamic strain instability associated with elliptical stream lines (Lebovitz & Lifschitz 1996), which raises concerns about the stability of certain types of geophysical flows and leads to suspicions about the evolutionary path of stars that are driven by gravitational-radiation-reaction (GRR) forces toward the Dedekind-sequence. In a recent nonlinear study of the secular bar-mode instability induced by GRR (Ou, Tohline, & Lindblom 2004), a uniformly rotating, axisymmetric neutron star, which was secularly unstable and driven by artificially enhanced GRR, evolved into a bar-like configuration with a very slow pattern speed. However, this special bar configuration became unstable to some kind of turbulence-like instability while evolving toward the Dedekind-sequence, that is, toward a stationary ellipsoidal structure in the inertial frame maintained purely by the internal motion of the fluid. It is suspected that this turbulence-like instability may be the elliptical strain instability identified in the earlier linear stability analyses. But no definite conclusion can be drawn because the stability of only one Dedekind-like configuration was studied. Following Ou, Tohline, & Lindblom (2004), one might consider generating additional ellipsoidal structures hydrodynamically, but the generation of each additional ellipsoidal model would be expensive in the sense that one has to evolve an initially axisymmetric model for a very long time, even with artificially enhanced GRR (Shibata & Karino 2004; Ou, Tohline, & Lindblom 2004). This approach would make it impractical to undertake a full stability investigation through the entire parameter space of ellipsoidal models.

Here we present a new 3D SCF technique that is capable of building the full range of incompressible Riemann S-type ellipsoids with nontrivial internal flows (i.e., not just the uniformly rotating Jacobi configurations, which are thought to be the end point of secularly unstable stars driven by viscosity, and stationary Dedekind configurations) as well as compressible triaxial models that share the same divergence-free velocity field as Riemann S-type ellipsoids. Our compressible models satisfy the steady-state Euler’s equation exactly, but only satisfy the steady-state continuity equation approximately, hence they are only in quasi-equilibrium. However, the violation of the steady-state continuity equation is very

small for nearly incompressible models, hence these models can be used effectively as initial configurations for a hydrodynamical study of the stability of compressible analogues of Riemann S-type ellipsoids. We note that, to date, hydrodynamical techniques have not been used to examine the stability of Riemann ellipsoids because the sound speed is formally infinite for incompressible models, while the time step in hydrodynamic codes is usually inversely proportional to the sound speed. On the other hand, since the elliptical strain instability associated with elliptical stream lines would set in on a dynamical time scale, we believe that our new “quasi-equilibrium” models will prove to be good starting points for hydrodynamical studies of this instability.

Our numerical method inherits one central idea of the traditional SCF method in that it makes use of the properties of the velocity field of Riemann S-type ellipsoids to turn the vector form of the steady-state Euler’s equation into a scalar form, thus yielding a uniform Bernoulli’s function. This enables us to follow the procedures of the traditional SCF method to use several boundary conditions to determine quantities elsewhere. To be concise, we will refer readers to Hachisu (1986a) and references therein for details of the traditional SCF technique, and focus on the new aspects of our new method.

2. Numerical Methods

Figure 1 reproduces key elements of a plot that Chandrasekhar (1969, see his chapter 7, figure 15) used to discuss sequences of Riemann S-type ellipsoids. In this $(b/a, c/a)$ parameter plot, a , b , and c are the three principal semiaxes of an ellipsoid, and each Riemann S-type ellipsoid with angular velocity ω and uniform vorticity ζ in the rotating frame resides between the two self-adjoint sequences (curves LP and LK) with $X = \mp 1$, where

$$X \equiv f \frac{ab}{a^2 + b^2}, \quad (1)$$

$$f \equiv \frac{\zeta}{\omega}. \quad (2)$$

The velocity field of a Riemann S-type ellipsoid as viewed from a frame rotating with angular velocity ω takes the following form:

$$\vec{v} = \lambda(ay/b, -bx/a, 0), \quad (3)$$

where λ is a constant that determines the magnitude of the internal motion of the fluid, and the origin of the x-y coordinate system is at the center of the ellipsoid. This velocity field \vec{v} is designed so that velocity vectors everywhere are always aligned with elliptical stream

lines by demanding that they be tangent to the equipotential contours, which are concentric ellipses.

Now, let's turn to a general self-gravitating system with some compressibility. If we adopt a polytropic equation of state, $p = k\rho^{1+1/n}$ (p is pressure, k is the polytropic constant and n is the polytropic index), Euler's equation for steady-state flows in the rotating frame is,

$$\vec{v} \cdot \nabla(\vec{v}) = -\nabla[H + \Phi - \frac{1}{2}\omega^2(x^2 + y^2)] - 2\vec{\omega} \times \vec{v}, \quad (4)$$

where H is enthalpy, and Φ is the gravitational potential. With the velocity field specified by Eq. (3), one can show that Eq. (4) is equivalent to the following equation,

$$\begin{aligned} -\nabla[\frac{1}{2}\lambda^2(x^2 + y^2)] &= -\nabla[H + \Phi - \frac{1}{2}\omega^2(x^2 + y^2)] \\ &\quad -\nabla[\omega\lambda(\frac{b}{a}x^2 + \frac{a}{b}y^2)]. \end{aligned} \quad (5)$$

Hence, within the configuration the following Bernoulli's function must be uniform in space:

$$\begin{aligned} H + \Phi - \frac{1}{2}\omega^2(x^2 + y^2) - \frac{1}{2}\lambda^2(x^2 + y^2) \\ + \omega\lambda(\frac{b}{a}x^2 + \frac{a}{b}y^2) = C_1, \end{aligned} \quad (6)$$

where C_1 is a constant. It should be mentioned that in this Bernoulli's function, ω and λ are interchangeable. This reflects the fact that, for any direct configuration ($\omega > \lambda$) in which fluid motion is dominated by figure rotation, the adjoint configuration ($\omega < \lambda$) in which fluid motion is dominated by internal motions can be obtained by simply interchanging ω and λ . We find it is useful to define an effective potential Φ_{eff} as:

$$\Phi_{\text{eff}} \equiv \Phi - \frac{1}{2}\omega^2(x^2 + y^2) - \frac{1}{2}\lambda^2(x^2 + y^2) + \omega\lambda(\frac{b}{a}x^2 + \frac{a}{b}y^2), \quad (7)$$

hence, the Bernoulli's function can also be written as:

$$H + \Phi_{\text{eff}} = C_1. \quad (8)$$

In our later discussion of equi-potential (iso-density) surfaces, we will often use the phrase “equi-potential” referring to Φ_{eff} .

On the other hand, the steady-state continuity equation in the rotating frame requires,

$$\nabla \cdot (\rho\vec{v}) = \rho\nabla \cdot \vec{v} + \vec{v} \cdot \nabla\rho = 0. \quad (9)$$

This is trivially satisfied for incompressible Riemann S-type ellipsoids because $\nabla \cdot \vec{v}$ is zero everywhere, and the velocity vectors in the rotating frame are always tangent to the concentric equi-potential contours and perpendicular to the unit vector that is normal to the

ellipsoidal surface. In our compressible models, the divergence-free velocity field given by Eq. (3) will continue to be adopted, so if the equi-potential (and iso-density) contours continue to be concentric ellipses (as assumed by Lai, Rasio & Shapiro 1993), the velocity vectors will always be orthogonal to the density gradient everywhere; this would satisfy the steady-state continuity equation exactly. However, as we demand that Euler’s equation be satisfied via the solution of Eq. (6), the iso-density contours for our compressible models are not guaranteed to be self-similar ellipses. Therefore, in our current numerical method, the extent to which the steady-state continuity equation is satisfied will depend on how far the density shells deviate from self-similar ellipses. For the remainder of this paper, we will only focus on obtaining a solution of Bernoulli’s function given by Eq. (6). We will return to issues related to the steady-state continuity equation in section 4.

For a given choice of axes (a, b, c) and a mass distribution $\rho(\vec{x})$ (hence $\Phi(\vec{x})$ is determined by Poisson’s equation), there are three unknown constants in Eq. (6): C_1 , ω and λ . On the other hand, we have three boundary conditions on the three axes at the surface of the star, i.e., points A, B and C as illustrated in Figure 2, where H drops to zero. (Note that points A, B and C are located on X , Y , and Z axes at $x = a$, $y = b$, and $z = c$, respectively.) These boundary conditions give the following equations:

$$\Phi_A - \frac{1}{2}a^2(\omega^2 + \lambda^2) + \omega\lambda ab = C_1, \quad (10)$$

$$\Phi_B - \frac{1}{2}b^2(\omega^2 + \lambda^2) + \omega\lambda ab = C_1, \quad (11)$$

$$\Phi_C = C_1. \quad (12)$$

Subtracting equation (11) from (10), we obtain

$$\omega^2 + \lambda^2 = \frac{2(\Phi_A - \Phi_B)}{a^2 - b^2}. \quad (13)$$

Adding equation (11) and (10) together, we obtain

$$\Phi_A + \Phi_B - 2\Phi_C = \frac{1}{2}[a^2(\omega^2 + \lambda^2) + b^2(\omega^2 + \lambda^2) - 4\omega\lambda ab]. \quad (14)$$

Since the right-hand-side of this last expression is non-negative, it follows that $\Phi_A + \Phi_B - 2\Phi_C \geq 0$. It can be shown that equations (13) and (14) are equivalent to equations (29) and (30) in Chapter 7 of Chandrasekhar (1969). The solutions of equations (13) and (14) for a direct configuration are:

$$\omega^2 = (M + \sqrt{M^2 - 4N^2})/2, \quad (15)$$

$$\lambda^2 = (M - \sqrt{M^2 - 4N^2})/2, \quad (16)$$

where

$$\begin{aligned} M &\equiv 2(\Phi_A - \Phi_B)/(a^2 - b^2), \\ N &\equiv \frac{(\Phi_A + \Phi_B - 2\Phi_C) - \frac{a^2+b^2}{a^2-b^2}(\Phi_A - \Phi_B)}{2ab}. \end{aligned}$$

For adjoint configurations, we only need to interchange ω^2 and λ^2 . The signs of ω and λ are determined by the sign of f (which is predetermined by the specified axis ratios), through Eq. (2) and the relationship,

$$\zeta = -\lambda(b/a + a/b). \quad (17)$$

With these constants and the Bernoulli’s function in hand, we can solve for H throughout the interior of the configuration.

In the incompressible case ($n = 0$), we know from the classical analytical results that the adopted velocity field generates equilibrium structures that are uniform density ellipsoids. Hence, we can obtain Riemann S-type ellipsoids directly by setting up a mass distribution that is confined by the ellipsoidal surface defined by three axes a , b and c ; then we solve Poisson’s equation to get the potential everywhere; finally, ω and λ can be determined by equations (15) and (16).

Compressible polytropic models ($n > 0$) having the same flow pattern as that of Riemann ellipsoids (given by Eq. 3), can also be constructed by an iterative procedure that is very similar to Hachisu’s SCF method (Hachisu 1986a). The main steps of this method include: (i) set up a trial ellipsoidal mass distribution defined by the choice of a , b , and c , then solve Poisson’s equation to obtain the gravitational potential everywhere (the details of our Poisson solver are discussed in Cohl & Tohline 1999); (ii) calculate C_1 , ω and λ using the three boundary conditions as discussed above; (iii) calculate the enthalpy everywhere inside the configuration using Eq. (6); (iv) calculate the new “trial” density distribution according to the relationship between the density and enthalpy for a polytrope. These steps are repeated until the model converges.

3. Results

In this section, we show our results for incompressible Riemann S-type ellipsoids and their quasi-equilibrium, compressible counterparts. Since the available parameter space occupies a large portion of Figure 1, we choose to build models only along the vertical dashed lines, which largely represent most of the configurations.

Our models are constructed on a cylindrical grid with a resolution of $66 \times 102 \times 128$ in the ϖ (cylindrical radius), z (vertical), and ϕ (azimuthal) directions, respectively. Following

Hachisu (1986a), we adopt a set of polytropic units in which the gravitational constant G , the radius of the entire grid ϖ_{grid} , and maximum density ρ_{max} are all set to 1. For all of our models, we set the semiaxis a to 0.619. We choose to present our results in such a way that readers can readily normalize our data to any unit system they are familiar with for the purpose of comparison. Table 1 shows the results for direct configurations of incompressible ($n = 0$) Riemann S-type ellipsoids. Tables 2, 3, and 4 show the same results but for compressible counterparts of Riemann ellipsoids with $n = 0.5$, $n = 1.0$, and $n = 1.5$, respectively. Tables 5, 6, and 7 show results for adjoint configurations with $n = 0.0$, $n = 0.5$ and $n = 1.0$, respectively.

In these tables, T is the rotational energy of the system, M_{tot} is the total mass, J_{tot} is the total angular momentum, ρ_{mean} is the mean density, W is the gravitational potential energy, and S is the thermal energy. The quantity $(S + T)/|W|$ measures how well our models are in virial equilibrium; ideally, this ratio should have a value of 0.5. All of our models have values that are very close to 0.5, especially for compressible configurations. In Table 1, the parameters ω_a and λ_a are analytically computed results for ω and λ , respectively.

Several properties of our models are worth discussing. First, for direct configurations with a fixed value of b/a , as one proceeds from larger values of c/a to smaller values, λ starts from a positive value, then continuously decreases; it reaches zero when the rigidly rotating Jacobi sequence is hit, and then becomes negative after passing the Jacobi sequence. The parameter f also switches sign when crossing the Jacobi/Dedekind sequences. For adjoint configurations, a similar behavior is observed for ω , while f approaches $\pm\infty$ around the Dedekind sequence because $\omega = 0$.

Second, in the parameter space above the Jacobi/Dedekind sequence where $f < 0$, ω is positive for direct configurations, and negative for adjoint configurations, which reflects the fact that the Jacobi mode in Maclaurin spheroids is the “forward moving” wave but the Dedekind mode is the “backward moving” wave. This also implies that in the adjoint configurations with $f < 0$, the ellipsoidal pattern is moving in a direction that is opposite to the overall rotation! Furthermore, when the critical Jacobi/Dedekind sequence is passed, f switches sign; so does λ in direct configurations and ω in adjoint configurations. In Maclaurin spheroids, this is where the frequency of the backward moving wave becomes positive in the inertial frame; hence, it is where the secular bar-mode instability sets in through gravitational radiation (Chandrasekhar-Friedman-Schutz instability) or viscosity (Chandrasekhar 1969; Friedman & Schutz 1978).

Finally, for softer equations of state, the SCF technique failed to converge to models with relatively small values of c/a because, in these cases, the centrifugal force at the boundary point A (see Figure 2) would exceed the gravitational force. In fact, for $n = 1$ and $n = 1.5$,

even the Jacobi sequence is not reached. This is consistent with previous studies that have indicated that the Jacobi sequence cannot exist for $n > 0.808$ (James 1964; Hachisu & Eriguchi 1982; Lai, Rasio & Shapiro 1993). Furthermore, as was pointed out by Hachisu & Eriguchi (1982) in their analysis of uniformly rotating polytropes, the mass-shedding limit never extends much beyond the bifurcation point (where the Jacobi/Dedekind sequence branches off the Maclaurin spheroid sequence) even for very small n : for $0.1 \leq n \leq 0.5$, this mass-shedding limit corresponds to $0.14 \leq T/|W| \leq 0.16$. Our $n = 0.5$ models are consistent with their results. Therefore, the available parameter space for compressible counterparts of Riemann ellipsoids becomes smaller as the equation of state becomes softer.

Figures 3 and 4 show equatorial-plane iso-density contours and velocity fields for direct and adjoint configurations of our $n = 0.5$ model with $b/a = 0.59$ and $c/a = 0.462$. Both the rotating frame velocity field \vec{v} and inertial frame velocity field $\vec{u} = \vec{v} + \vec{\omega} \times \vec{r}$ are plotted for comparison. The flow patterns in these two models are different from each other although they have identical geometrical shapes. It is also clear that the fluid motion in the adjoint configuration is dominated by internal motion rather than rotation. As another illustration, Figures 5 and 6 illustrate the structure of our $n = 1$ model with $b/a = 0.59$ and $c/a = 0.564$. Notice that ω , which is also the pattern speed of the ellipsoid, is negative in both Fig. 4 and Fig. 6, so the ellipsoidal figures in both plots are spinning retrograde (clockwise) relative to the overall fluid rotation.

Comparisons between previous published results and our models yield very good agreement. For example, from Table IV in Chapter 6 of Chandrasekhar (1969), a Jacobi ellipsoid with $\lambda = 0$ and $b/a = 0.60$, $c/a = 0.434$, has $\omega^2/(\pi G\rho) = 0.3373$ and $J_{\text{tot}}/\sqrt{GM_{\text{tot}}^3 \bar{a}} = 0.3356$, where $\bar{a} = (abc)^{1/3}$. The closest match among our models shown in Table 1, with $b/a = 0.59$, $c/a = 0.436$, has $\omega^2/(\pi G\rho) = 0.3370$, $J_{\text{tot}}/\sqrt{(GM_{\text{tot}}^3 \bar{a})} = 0.3321$, and an almost vanishing $\lambda = 0.0108$, which shows that this model from our Table is very close to the Jacobi sequence. It should be noticed that, due to the discrete nature of our grid, we cannot construct models with axis ratios that will place the models precisely on the Jacobi/Dedekind sequence, but we can construct models that are very close to this sequence (with very small values of λ or ω). As another comparison, the last four columns in Table 1 give analytically computed results of ω_a and λ_a for Riemann S-type ellipsoids having the specified axes ratios b/a and c/a , as well as the ratio between numerical and analytical results (only models with $a < b < c$ have been computed). To obtain these analytical results, we used standard incomplete elliptic integrals to evaluate the potential field of a homogeneous ellipsoid (Binney & Tremaine 1987, see their Table 2-2). In virtually all cases, the error in ω is \lesssim a few percent. On the other hand, for the direct configurations the fractional error in λ can be as large as 50%; the error is largest for models whose λ almost vanishes. This is understandable because a small variation in the magnitude of λ will result in a large percentage difference when λ is

approaching zero. Also some mismatch between numerical and analytical results may arise because the discrete nature of our grids makes it difficult for us to define an exact axis ratio for our models.

For compressible equations of state, we can compare our results with those presented by Lai, Rasio & Shapiro (1993), who used an energy variational method to determine approximate equilibrium configurations for ellipsoidal self-gravitating systems. Lai, Rasio & Shapiro (1993) assumed that the iso-density contours of each configuration are self-similar concentric ellipses, which as we have already emphasized is not the case. In their Table 4, for compressible analogues of Jacobi ellipsoids, a configuration with $b/a = 0.75$ and $c/a = 0.4983$ has $T/|W| = 0.1407$; the closest match among our $n = 0.5$ models (see Table 2) with $b/a = 0.74$ and $c/a = 0.487$ has $T/|W| = 0.135$. Other quantities also match well, after a proper normalization is applied as prescribed by their equation (3.27). We omit more comparisons here and leave the rest to interested readers.

Other models that are of interest are the $f = -2$ irrotational sequence (Uryu & Eriguchi 1998). It turns out that the f parameter is very sensitive to the axis ratios, so we could not build models that are very close to the irrotational sequence due to the discrete nature of our computational grids. Our model that comes closest has $f = -1.9$; it is a direct configuration with $n = 0.5$ and its other parameters are listed in Table 2.

4. Discussion and Future Work

We have presented a new method to construct 3D models for Riemann S-type ellipsoids ($n = 0$), and the method has been extended to construct compressible counterparts that share the same velocity field as that of Riemann S-type ellipsoids. With this method, we have been able to build 3D models that cover almost the entire parameter space of Riemann S-type ellipsoids. Our results are in good agreement with previous studies. We expect that this method can also be straightforwardly extended to the construction of Roche-Riemann ellipsoids.

By design, our compressible models satisfy the steady-state Euler’s equation. However, it is not guaranteed that they simultaneously satisfy the steady-state continuity equation exactly, because this additional constraint was not built into our method. Because the adopted velocity flow-field \vec{v} in our models is divergence-free, the violations of the steady-state continuity equation will only arise to the extent that the iso-density contours deviate from concentric ellipses. As we can see from Figures 3 - 6, the outer low-density shell in compressible models becomes somewhat pointed along the major axis. However, the

deviation from concentric ellipses is small and almost negligible in the inner, high-density regions. Furthermore, a comparison between Fig. 3 and Fig. 5 shows that this deviation becomes smaller in less compressible models. In order to quantitatively measure the violation of the steady-state continuity equation, we calculated $|\dot{\rho}|/\rho \equiv |\nabla \cdot (\rho \vec{v})|/\rho$ for the models shown in Figs 3, 4, and 5. As long as $|\dot{\rho}|/\rho \ll \sqrt{\pi G \rho_{max}} = \sqrt{\pi}$ for a given configuration, we can consider that the model has a reasonably good quasi-equilibrium structure. In Figure 7, we have plotted $|\dot{\rho}|/\rho$ in the equatorial plane as a function of cylindrical radius ϖ along different azimuthal angles, $\phi = \pi/8$ and $\phi = \pi/4$. In fact, this quantity remains small ($\lesssim 0.01$ for $n = 0.5$ and $\lesssim 0.1$ for $n = 1.0$) throughout the majority of the configuration, but not surprisingly near the surface it asymptotically approaches infinity because ρ goes to zero. As the figure illustrates, $|\dot{\rho}|/\rho$ is smaller for the stiffer equation of state. We also note that $|\dot{\rho}|/\rho$ is nearly zero along the X and Y axes because the velocity vectors in the rotating frame along the X (Y) axis only have a nonzero Y (X) component and are therefore perpendicular to the density gradient there. Thus, we expect our compressible models to represent fairly good quasi-equilibrium configurations, especially in nearly incompressible cases.

On the other hand, this point was brought to our attention by an anonymous referee: the relatively large violation of the steady-state continuity equation on the very surface layer can potentially change the shape of the surface in hydrodynamical evolutions. To understand how the shape of the surface might be changed by the flow field, it is important to know the sign of $\nabla \cdot (\rho \vec{v})/\rho$ along the surface. Since we are adopting a divergence free velocity field, the sign of $\nabla \cdot (\rho \vec{v})/\rho$ is determined by the sign of $\vec{v} \cdot \nabla \rho$, which also measures to what degree the velocity vectors are orthogonal to density gradient. If the velocity vector points slightly outward (inward) from the surface, $\vec{v} \cdot \nabla \rho$ will be negative (positive), because the density gradient is negative outward. Figs. 8 and 9 show contour maps of $\nabla \cdot (\rho \vec{v})/\rho$ in the equatorial planes of the direct and adjoint models shown in Figs. 3 and 4, respectively. (We note that the contour pattern for direct configurations will switch from Fig. 8 to Fig. 9 if λ flips sign.) A π symmetry is observed for both patterns. We also note that, in each quadrant, $\nabla \cdot (\rho \vec{v})/\rho$ flips sign, which implies that the direction of velocity vectors will change from inward (outward) to outward (inward) from the surface within one single quadrant. Accordingly, Fig. 10 shows a combined schematic drawing of how the velocity vectors in the rotating frames are aligned with the surface for these two patterns (the panel on the left is for the adjoint figure shown in Fig. 4, the panel on the right is for the direct figure shown in Fig. 3). In this figure, the black ellipse denotes the actual surface (which should not be a perfect ellipse), red arrows denote velocity vectors on the surface, purple arrows denote density gradient vectors, which are drawn pointing inward because of their negative sign. For direct configurations, in which the figure rotation is larger than the internal motion, these mismatches (nonvanishing $\vec{v} \cdot \nabla \rho$) on top of a large rotation are likely to generate spiral

arms; whereas, for adjoint configurations, the internal motion is larger than figure rotation, so these mismatches tend to generate waves along the surface.

Using the 3D hydrodynamics code developed by the LSU group (Motl, Tohline, & Frank 2002), we have carried out nonlinear 3D hydrodynamical evolutions for a subset of the nearly incompressible models discussed here in Table 2. Despite the fact that the models do not fully satisfy the steady-state continuity equation, they are in very good force-balance initially and, as predicted by the above discussion, the models are fairly long-lived, holding their initial ellipsoidal shapes over the time that is followed by our simulations (~ 15 - 20 dynamical times). We also observed the formation of narrow spiral arms (low amplitude surface waves) containing low density materials in direct (adjoint) configurations. The results of these hydrodynamical evolutions will be presented in a separate paper in the context of our ongoing study of the stability of Riemann S-type ellipsoids. Since our ellipsoidal models are fairly long-lived and have exactly the same elliptical flow field as Riemann S-type ellipsoids, they should provide good initial states for a nonlinear, hydrodynamical study of dynamical instabilities in Riemann S-type ellipsoids. We especially have in mind the elliptical strain instability that is associated with elliptical stream lines, which should set in on a dynamical time scale. Through such a study, we hope to provide insight into the stability of ellipsoidal configurations that will complement the work of Lebovitz & Lifschitz (1996). This should also help answer whether the evolutionary path of a GRR-driven star toward the Dedekind sequence is viable.

I would like to thank Joel Tohline for valuable suggestions, discussions and carefully reading through this paper. I also thank Juhan Frank and Patrick Motl for helpful comments. It is a pleasure to thank Norman Lebovitz for drawing our attention to the particular analytical expression of the velocity field of Riemann S-type ellipsoids used in this study. I would also thank Howard Cohl for developing the Poisson solver that was an important ingredient in this work. I thank the anonymous referee for insightful suggestions to analysis our models. This work was partially supported by NSF grants AST-0407070 and PHY-0326311, and by the Center for Computation & Technology at LSU.

REFERENCES

- Binney, J., & Tremaine, S., 1987, *Galactic Dynamics*, New York: Academic Press
- Cazes, J. E., & Tohline, J. E. 2000, *ApJ*, 532, 1051

- Chandrasekhar, S. 1969, *Equilibrium Figures of Equilibrium*, New Haven, CT: Yale Univ. Press
- Cohl, H. S., & Tohline, J. E. 1999, *ApJ*, 527, 86
- Friedman, J., & Schutz, B. F. 1978, *ApJ*, 222, 281
- Hachisu, I. 1986, *ApJS*, 61, 479
- Hachisu, I. 1986, *ApJS*, 62, 461
- Hachisu, I., Eriguchi, Y., 1982, *Prog. Theor.Phys.*, 68, 206
- Hachisu, I., Eriguchi, Y., 1984, *PASJ*, 36, 239
- James, R. A., 1964, *ApJ*, 140, 552
- Lai, D., Rasio, F. A., & Shapiro, S. L. 1993, *ApJS*, 88, 205
- Lai, D., & Shapiro, S. L. 1995, *ApJ*, 442, 259
- Lebovitz, N. R., & Lifschitz, A. 1996, *ApJ*, 458, 699
- Lebovitz, N. R., & Saldanha, K. I. 1999, *Physics of Fluids*, 11, 3374
- Lifschitz, A., & Lebovitz, N. 1993, *ApJ*, 408, 603
- Motl, P. M., Tohline, J. E., & Frank, J. 2002, *ApJS*, 138, 121
- Ostriker, J.P., Mark, J. W.-K., 1968, *ApJ*, 151, 1075
- Ou, S., Tohline, J. E., & Lindblom, L. 2004, *ApJ*, 617, 490
- Shibata, M., & Karino, S., 2004, *Phys. Rev. D*, 70, 084022
- Shibata, M., Karino, S., & Eriguchi, Y. 2002, *MNRAS*, 334,L27
- Tohline, J. E., Durisen, R. H., & McCollough, M. 1985, *ApJ*, 298, 220
- Uryu, K., & Eriguchi, Y., 1996, *MNRAS*, 282, 653
- Uryu, K., & Eriguchi, Y., 1998, *ApJS*, 118, 563
- Williams, H. A., & Tohline, J. E. 1988, *ApJ*, 334, 449

Table 1. Direct Configurations of Riemann S-type Ellipsoids ($n = 0$)

b/a	c/a	ω	λ	$T/ W $	J_{tot}	M_{tot}	W	$(S + T)/ W $	f	ω_a	ω/ω_a	λ_a	λ/λ_a
0.90	0.923	1.030	0.7550	6.6e-3	0.03183	0.8232	-0.6989	0.4989	-1.5				
0.90	0.795	1.144	0.4310	0.046	0.07018	0.7086	-0.5429	0.4992	-0.76	1.14704	0.997	0.43181	0.998
0.90	0.641	1.119	0.1394	0.101	0.07764	0.5720	-0.3759	0.4988	-0.25	1.13137	0.989	0.15077	0.925
0.90	0.590	1.099	0.0569	0.122	0.07589	0.5261	-0.3249	0.4987	-0.10	1.10661	0.993	0.06406	0.888
0.90	0.564	1.090	0.0210	0.132	0.07452	0.5033	-0.3007	0.4989	-0.04	1.09034	0.999	0.02033	1.033
0.90	0.538	1.069	-0.0250	0.144	0.07268	0.4801	-0.2768	0.4991	0.05	1.07148	0.998	-0.02324	1.075
0.90	0.487	1.015	-0.1205	0.167	0.06814	0.4341	-0.2316	0.4992	0.24	1.02639	0.989	-0.10880	1.108
0.90	0.333	0.797	-0.3885	0.246	0.04860	0.2970	-0.1167	0.4983	0.98	0.79257	1.006	-0.39224	0.990
0.74	0.769	1.099	0.5604	0.030	0.03807	0.5682	-0.3744	0.4982	-1.1				
0.74	0.692	1.133	0.3840	0.058	0.04678	0.5116	-0.3134	0.4986	-0.71	1.13215	1.001	0.38599	0.995
0.74	0.538	1.094	0.0774	0.121	0.04836	0.3982	-0.2034	0.4990	-0.15	1.09508	0.999	0.08149	0.950
0.74	0.513	1.078	0.0303	0.133	0.04734	0.3791	-0.1857	0.4991	-0.06	1.07883	0.999	0.03474	0.872
0.74	0.487	1.054	-0.0208	0.145	0.04594	0.3560	-0.1700	0.4988	0.04	1.05883	0.995	-0.01363	1.526
0.74	0.436	1.003	-0.1184	0.171	0.04284	0.3223	-0.1400	0.4987	0.25	1.00963	0.993	-0.10852	1.091
0.74	0.333	0.847	-0.3230	0.228	0.03389	0.2463	-0.0863	0.4983	0.80	0.85686	0.988	-0.31006	1.042
0.74	0.282	0.715	-0.4523	0.259	0.02842	0.2081	-0.0634	0.4968	1.3	0.72756	0.983	-0.43781	1.033
0.59	0.718	0.948	0.7677	0.014	0.01197	0.4208	-0.2243	0.4924	-1.9				
0.59	0.538	1.087	0.2338	0.093	0.02876	0.3157	-0.1374	0.4982	-0.49	1.08732	0.999	0.23529	0.994
0.59	0.436	1.029	0.0108	0.145	0.02691	0.2554	-0.0949	0.4985	-0.02	1.03198	0.997	0.01472	0.734
0.59	0.410	1.008	-0.0417	0.159	0.02592	0.2404	-0.0853	0.4991	0.09	1.00774	1.000	-0.04012	1.039
0.59	0.359	0.943	-0.1534	0.188	0.02342	0.2104	-0.0673	0.4989	0.37	0.94638	0.996	-0.14830	1.034
0.59	0.231	0.584	-0.5426	0.267	0.01475	0.1351	-0.0300	0.4910	2.1	0.60698	0.962	-0.51563	1.013
0.41	0.385	0.971	0.1369	0.132	0.01220	0.1563	-0.0407	0.4978	-0.40	0.97108	1.000	0.14159	0.967
0.41	0.333	0.930	0.0016	0.165	0.01112	0.1347	-0.0313	0.4998	-0.005	0.92963	1.000	0.00331	0.483
0.41	0.308	0.900	-0.0685	0.183	0.01061	0.1254	-0.0275	0.4991	0.22	0.89982	1.000	-0.06224	1.101
0.41	0.256	0.808	-0.2074	0.217	0.00896	0.1046	-0.0199	0.4937	0.73	0.81275	0.994	-0.20138	1.030
0.28	0.256	0.809	0.0246	0.183	0.00472	0.0717	-0.0103	0.4982	-0.12	0.80944	0.999	0.03668	0.671
0.28	0.231	0.780	-0.0572	0.204	0.00431	0.0646	-0.0086	0.4988	0.28	0.77651	1.004	-0.04714	1.213
0.28	0.205	0.726	-0.1505	0.224	0.00382	0.0575	-0.0069	0.4967	0.80	0.72853	0.996	-0.13511	1.114

Table 2. Direct Configurations with $n = 0.5$

b/a	c/a	ω	λ	$T/ W $	J_{tot}	M_{tot}	ρ_{mean}	W	$(S + T)/ W $	f
0.90	0.795	0.970	0.3660	0.045	0.0258	0.3812	0.5398	-0.1751	0.5000	-0.76
0.90	0.744	0.975	0.2831	0.061	0.0273	0.3541	0.5371	-0.1544	0.5000	-0.58
0.90	0.692	0.970	0.2050	0.079	0.0276	0.3266	0.5344	-0.1344	0.5001	-0.43
0.90	0.641	0.958	0.1312	0.097	0.0227	0.2987	0.5309	-0.1150	0.5001	-0.28
0.90	0.590	0.940	0.0617	0.117	0.0256	0.2695	0.5263	-0.0964	0.5001	-0.13
0.90	0.564	0.929	0.0287	0.127	0.0246	0.2546	0.5240	-0.0873	0.5001	-0.06
0.90	0.538	0.920	0.0001	0.137	0.0233	0.2391	0.5198	-0.0783	0.5001	-0.0002
0.90	0.513	0.908	-0.0281	0.147	0.0218	0.2234	0.5169	-0.0695	0.5001	0.06
0.90	0.487	0.898	-0.0513	0.157	0.0201	0.2066	0.5115	-0.0607	0.5001	0.12
0.74	0.692	0.958	0.3232	0.055	0.0166	0.2719	0.5380	-0.0991	0.4997	-0.71
0.74	0.641	0.959	0.2343	0.074	0.0171	0.2489	0.5345	-0.0852	0.4999	-0.51
0.74	0.590	0.949	0.1514	0.094	0.0167	0.2252	0.5314	-0.0717	0.5001	-0.33
0.74	0.538	0.932	0.0750	0.114	0.0156	0.2005	0.5263	-0.0587	0.5001	-0.17
0.74	0.487	0.911	0.0081	0.135	0.0137	0.1737	0.5192	-0.0458	0.5002	-0.02
0.74	0.462	0.904	-0.0171	0.144	0.0123	0.1588	0.5156	-0.0393	0.5002	0.04
0.59	0.718	0.792	0.6631	0.012	0.0037	0.2241	0.5418	-0.0713	0.4943	-1.9
0.59	0.538	0.922	0.2021	0.085	0.0090	0.1587	0.5304	-0.0397	0.4997	-0.50
0.59	0.487	0.911	0.1137	0.105	0.0081	0.1373	0.5256	-0.0313	0.5001	-0.29
0.59	0.462	0.905	0.0754	0.114	0.0073	0.1250	0.5230	-0.0265	0.5002	-0.19
0.59	0.436	0.871	-0.0337	0.153	0.0105	0.1382	0.5453	-0.0031	0.5088	0.09

Table 3. Direct Configurations with $n = 1.0$

b/a	c/a	ω	λ	$T/ W $	J_{tot}	M_{tot}	ρ_{mean}	W	$(S + T)/ W $	f
0.90	0.795	0.803	0.3029	0.039	0.00893	0.2053	0.2921	-0.0577	0.5001	-0.76
0.90	0.744	0.804	0.2329	0.053	0.00910	0.1870	0.2867	-0.0492	0.5001	-0.58
0.90	0.692	0.796	0.1684	0.067	0.00872	0.1679	0.2799	-0.0409	0.5002	-0.43
0.90	0.641	0.782	0.1090	0.081	0.00788	0.1476	0.2711	-0.0328	0.5002	-0.28
0.90	0.590	0.760	0.0555	0.093	0.00657	0.1255	0.2611	-0.0249	0.5002	-0.14
0.90	0.564	0.747	0.0314	0.097	0.00572	0.1134	0.2563	-0.0210	0.5002	-0.08
0.74	0.641	0.784	0.1917	0.060	0.00513	0.1262	0.2805	-0.0254	0.5003	-0.51
0.74	0.590	0.769	0.1241	0.074	0.00450	0.1087	0.2731	-0.0197	0.5003	-0.34
0.74	0.538	0.743	0.0626	0.084	0.00349	0.0893	0.2680	-0.0143	0.5003	-0.18
0.74	0.512	0.722	0.0322	0.086	0.00289	0.0786	0.2676	-0.0115	0.5003	-0.09
0.59	0.590	0.748	0.244	0.046	0.00237	0.0870	0.2836	-0.0136	0.5007	-0.75
0.59	0.564	0.743	0.2011	0.052	0.00220	0.0797	0.2817	-0.0118	0.5009	-0.62

Table 4. Direct Configurations with $n = 1.5$

b/a	c/a	ω	λ	$T/ W $	J_{tot}	M_{tot}	ρ_{mean}	W	$(S + T)/ W $	f
0.90	0.795	0.631	0.2351	0.030	0.00273	0.1068	0.1531	-0.0181	0.5002	-0.75
0.90	0.744	0.622	0.1752	0.040	0.00260	0.0945	0.1467	-0.0147	0.5003	-0.57
0.90	0.692	0.604	0.1187	0.048	0.00229	0.0817	0.1397	-0.0115	0.5003	-0.40
0.90	0.641	0.574	0.0640	0.055	0.00183	0.0683	0.1324	-0.0085	0.5003	-0.22
0.90	0.615	0.554	0.0365	0.057	0.00157	0.0614	0.1292	-0.00711	0.5003	-0.13
0.74	0.692	0.609	0.2024	0.033	0.00148	0.0717	0.1491	-0.00931	0.5006	-0.70
0.74	0.641	0.592	0.1378	0.041	0.00130	0.0612	0.1430	-0.00713	0.5005	-0.49
0.64	0.670	0.587	0.2503	0.023	0.00086	0.0586	0.1524	-0.00666	0.5014	-0.94
0.64	0.640	0.584	0.2116	0.027	0.00084	0.0542	0.1499	-0.00584	0.5013	-0.80

Table 5. Adjoint Configurations of Riemann S-type Ellipsoids ($n = 0$)

b/a	c/a	ω	λ	$T/ W $	J_{tot}	M_{tot}	ρ_{mean}	W	$(S + T)/ W $	f
0.90	0.923	-0.755	-1.030	0.0064	0.0307	0.8232	0.99999	-0.6989	0.4987	-2.744
0.90	0.641	-0.139	-1.119	0.100	0.0770	0.572	0.99999	-0.3758	0.4980	-16.1
0.90	0.590	-0.0569	-1.099	0.121	0.0754	0.5261	0.99999	-0.3249	0.4979	-38.8
0.90	0.564	-0.0211	-1.090	0.132	0.0741	0.5033	0.99999	-0.3007	0.4981	-104.2
0.90	0.538	0.0250	-1.069	0.143	0.0723	0.4801	0.99999	-0.2768	0.4982	86.0
0.90	0.487	0.121	-1.015	0.166	0.0678	0.4342	0.99999	-0.2314	0.4983	16.9
0.90	0.436	0.219	-0.945	0.191	0.0623	0.3886	0.99999	-0.1900	0.4979	8.689
0.90	0.333	0.389	-0.797	0.246	0.0485	0.2970	0.99999	-0.1167	0.4978	4.128
0.74	0.744	-0.495	-1.117	0.035	0.0376	0.5496	0.99999	-0.3540	0.4943	-4.7
0.74	0.590	-0.171	-1.116	0.093	0.0465	0.4357	0.99999	-0.2377	0.4933	-13.6
0.74	0.513	-0.030	-1.078	0.127	0.0452	0.3791	0.99999	-0.1866	0.4932	-74.3
0.74	0.487	0.021	-1.054	0.139	0.0440	0.3595	0.99999	-0.1699	0.4928	106.8
0.74	0.436	0.118	-1.002	0.165	0.0414	0.3223	0.99999	-0.1400	0.4929	17.7
0.74	0.385	0.210	-0.944	0.193	0.0376	0.2841	0.99999	-0.1117	0.4934	9.4
0.74	0.333	0.323	-0.847	0.223	0.0332	0.2463	0.99999	-0.0863	0.4940	5.5
0.74	0.282	0.453	-0.714	0.257	0.0281	0.2081	0.99999	-0.0634	0.4944	3.4
0.59	0.615	-0.417	-1.085	0.045	0.0199	0.3608	0.99999	-0.1729	0.4834	-5.5
0.59	0.487	-0.119	-1.063	0.100	0.0239	0.2853	0.99999	-0.1152	0.4807	-20.4
0.59	0.436	-0.011	-1.029	0.126	0.0235	0.2553	0.99999	-0.0949	0.4801	-217.5
0.59	0.410	0.042	-1.008	0.140	0.0229	0.2404	0.99999	-0.0853	0.4807	55.2
0.59	0.359	0.153	-0.943	0.170	0.0213	0.2104	0.99999	-0.0672	0.4811	14.1
0.59	0.282	0.271	-0.856	0.204	0.0190	0.1803	0.99999	-0.0509	0.4822	7.2
0.59	0.231	0.402	-0.729	0.242	0.0161	0.1502	0.99999	-0.0365	0.4843	4.1

Table 6. Adjoint Configurations with $n = 0.5$

b/a	c/a	ω	λ	$T/ W $	J_{tot}	M_{tot}	ρ_{mean}	W	$(S + T)/ W $	f
0.90	0.923	-0.642	-0.8766	0.0063	0.0116	0.4476	0.5442	-0.2297	0.4997	-2.7
0.90	0.590	-0.062	-0.9401	0.116	0.0255	0.2695	0.5263	-0.0964	0.4997	-30.7
0.90	0.538	-1.47e-4	-0.9195	0.137	0.0232	0.2391	0.5197	-0.0782	0.4999	-12606.1
0.90	0.513	0.028	-0.9080	0.147	0.0218	0.2234	0.5169	-0.0695	0.5000	65.2
0.74	0.795	-0.537	-0.9101	0.018	0.0102	0.3167	0.5421	-0.1283	0.4966	-3.5
0.74	0.692	-0.323	-0.9584	0.052	0.0154	0.2719	0.5379	-0.0991	0.4963	-6.2
0.74	0.538	-0.075	-0.9317	0.112	0.0150	0.2005	0.5263	-0.0587	0.4975	-25.9
0.74	0.487	-8.2e-3	-0.9114	0.134	0.0133	0.1737	0.5192	-0.0458	0.4992	-233.1
0.74	0.462	0.0171	-0.9044	0.145	0.0121	0.1587	0.5157	-0.0393	0.5009	110.2
0.59	0.615	-0.355	-0.9180	0.044	6.93e-3	0.1877	0.5368	-0.0529	0.4894	-5.9
0.59	0.538	-0.202	-0.9222	0.076	7.66e-3	0.1587	0.5304	-0.0397	0.4910	-10.4
0.59	0.487	-0.114	-0.9111	0.100	7.21e-3	0.1373	0.5256	-0.0310	0.4948	-18.3
0.59	0.462	-0.075	-0.9050	0.113	6.65e-3	0.1250	0.5230	-0.0265	0.4992	-27.4

Table 7. Adjoint Configurations with $n = 1.0$

b/a	c/a	ω	λ	$T/ W $	J_{tot}	M_{tot}	ρ_{mean}	W	$(S + T)/ W $	f
0.90	0.795	-0.303	-0.8030	0.039	0.00887	0.2053	0.2921	-0.0577	0.5000	-5.33
0.90	0.692	-0.168	-0.7963	0.067	0.00869	0.1679	0.2799	-0.0409	0.5003	-9.51
0.90	0.590	-0.056	-0.7605	0.094	0.00657	0.1255	0.2611	-0.0249	0.5009	-27.59
0.90	0.564	-0.031	-0.7469	0.099	0.00573	0.1134	0.2563	-0.0210	0.5014	-47.78
0.74	0.641	-0.192	-0.7842	0.061	0.00499	0.1262	0.2805	-0.0254	0.5013	-8.54
0.74	0.538	-0.062	-0.7429	0.091	0.00354	0.0893	0.2680	-0.0142	0.5071	-24.80
0.74	0.512	-0.032	-0.7220	0.096	0.00295	0.0786	0.2676	-0.0115	0.5097	-46.74
0.59	0.590	-0.244	-0.7480	0.050	0.00217	0.0870	0.2836	-0.0136	0.5049	-7.01
0.59	0.564	-0.201	-0.7433	0.059	0.00210	0.0797	0.2817	-0.0118	0.5083	-8.47

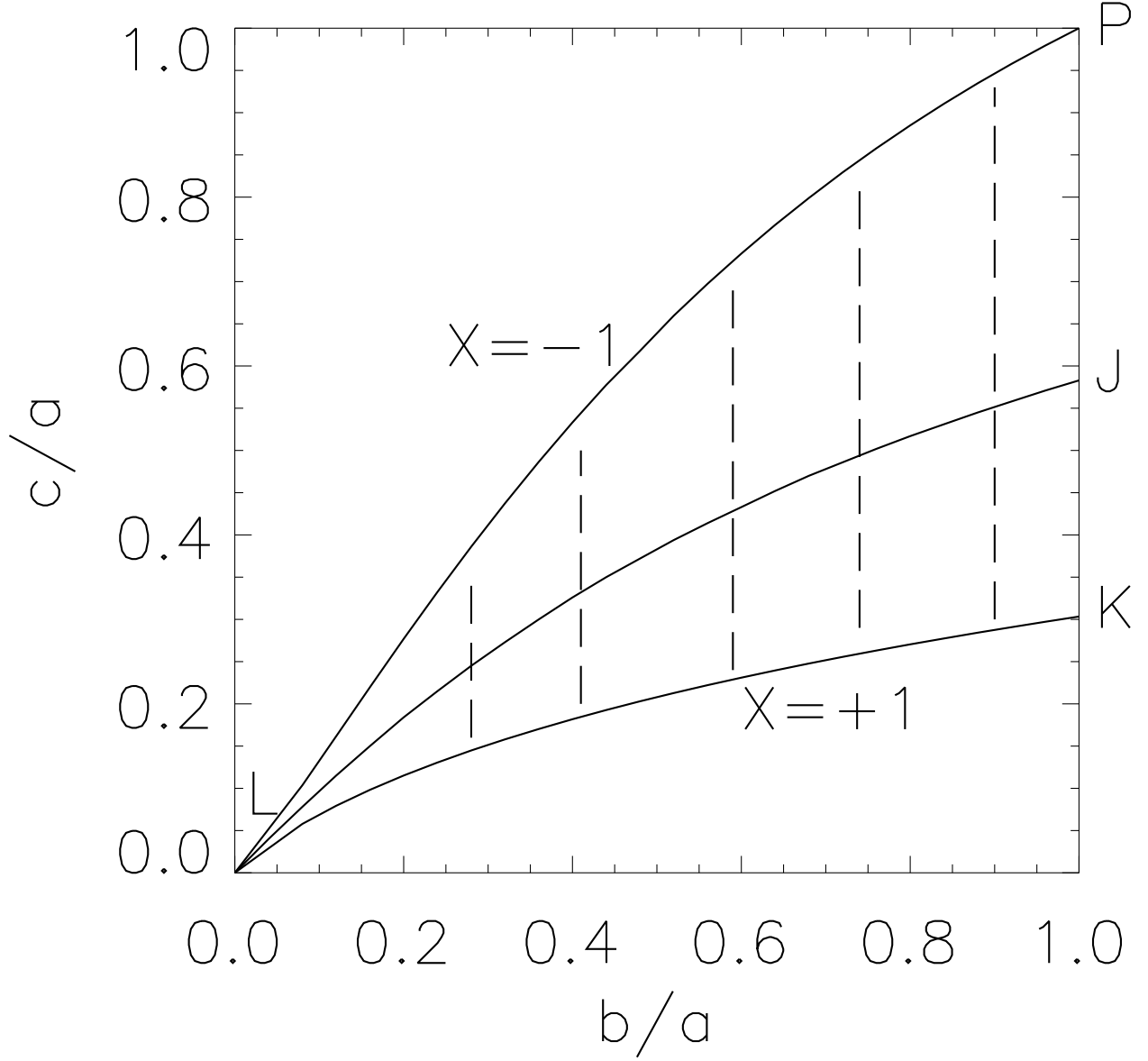


Fig. 1.— Parameter space of Riemann S-type ellipsoids on a $(b/a, c/a)$ plot. Curve LJ denotes for the Jacobi/Dedekind sequence, curves LP and LK are the two self-adjoint sequences with $X = \mp 1$. Models are constructed along dashed lines in order to cover most of the parameter space.

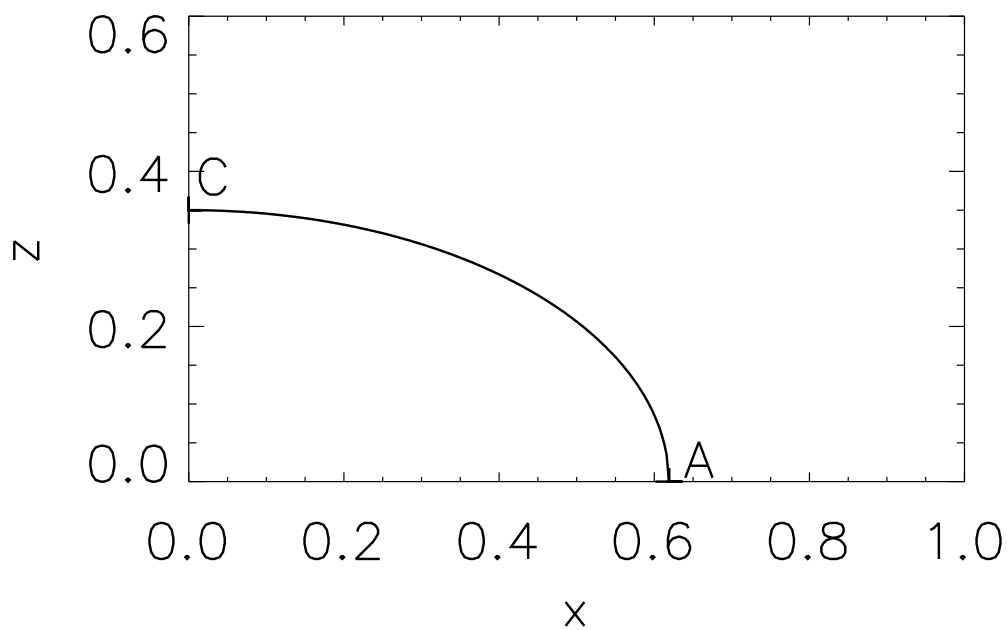
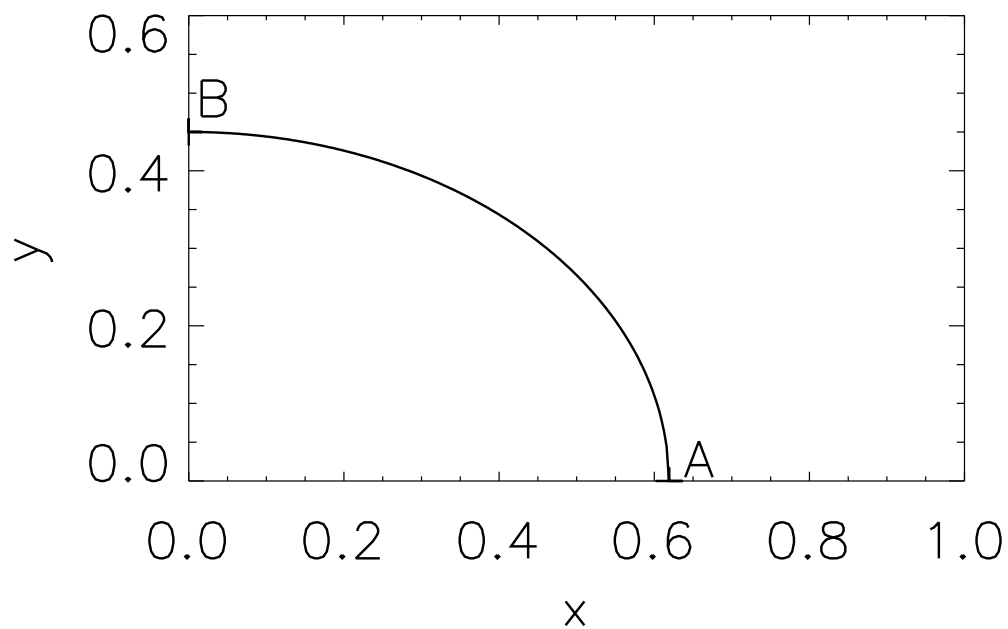


Fig. 2.— Three boundary conditions at the surfaces of an ellipsoid. Solid lines are part of the elliptical surface.

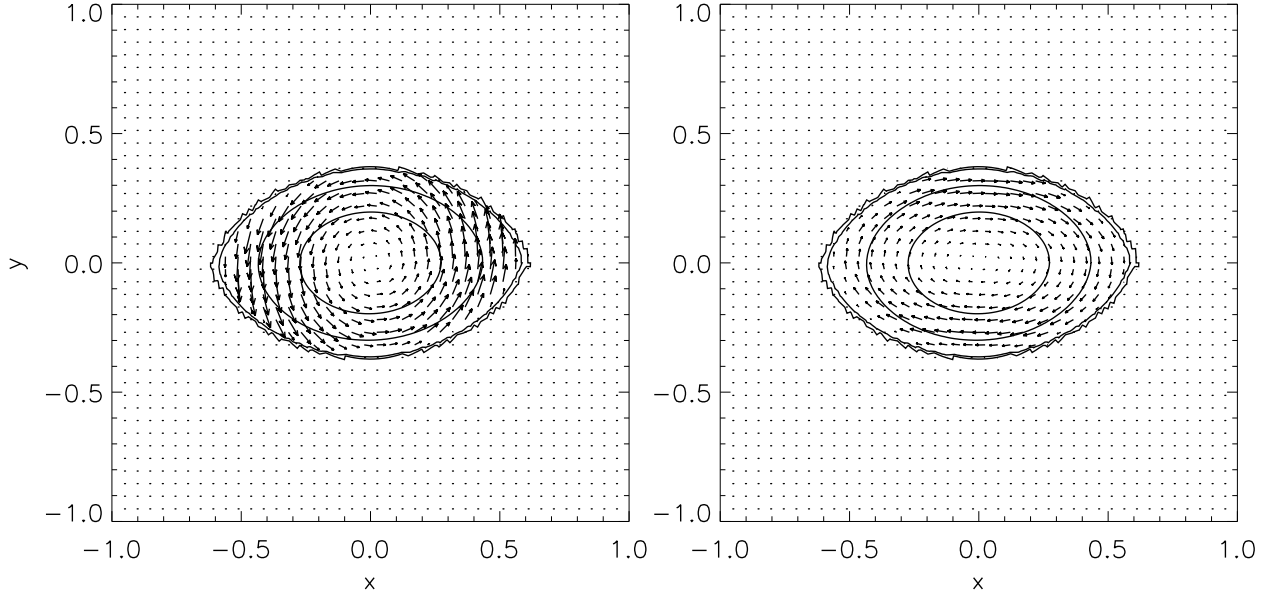


Fig. 3.— Equatorial iso-density contours and velocity fields in the inertial frame (left) and rotating frame (right) for an $n = 0.5$, direct configuration with $b/a = 0.59$ and $c/a = 0.462$. Density contours correspond to $\rho/\rho_{max} = 0.01, 0.1, 0.5, 0.8$ from the outermost shell to innermost shell. This model has $\omega = 0.905$ and $\lambda = 0.0754$, which corresponds to a vorticity $\zeta = -0.17$ in the rotating frame. So the ellipsoidal configuration is spinning prograde (in the same direction as the overall fluid rotation, i.e., counterclockwise) rapidly in the inertial frame, but the fluid is moving more slowly and retrograde as viewed from the rotating frame.

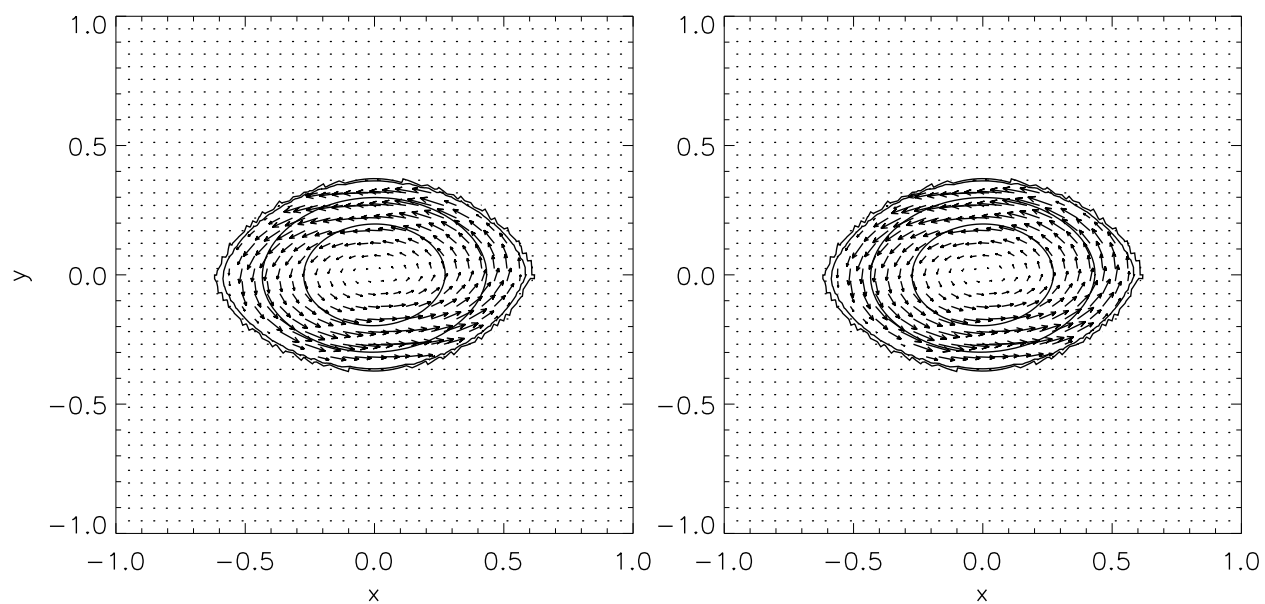


Fig. 4.— The same as Fig. 3 but for the adjoint configuration. This model has $\omega = -0.075$ and $\lambda = -0.905$, which corresponds to $\zeta = 2.07$, so the ellipsoidal configuration has a slow retrograde (clockwise) spin in the inertial frame (left), but the fluid is moving rapidly prograde as viewed from the rotating frame (right).

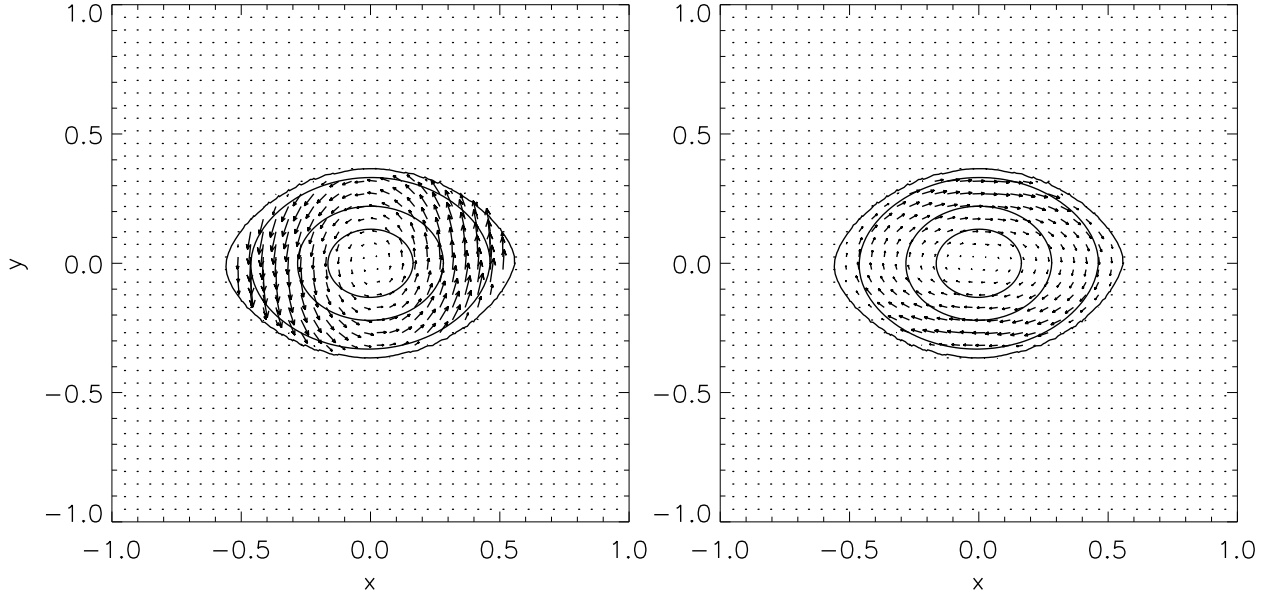


Fig. 5.— The same as Fig. 3 but for an $n = 1$, direct configuration with $b/a = 0.59$ and $c/a = 0.564$. Density contours correspond to $\rho/\rho_{max} = 0.01, 0.1, 0.5, 0.8$ from the outermost shell to innermost shell. This model has $\omega = 0.743$ and $\lambda = 0.2011$, which corresponds to $\zeta = -0.46$. So the ellipsoidal configuration is spinning prograde (counterclockwise) rapidly in the inertial frame (left), but the fluid is moving retrograde (clockwise) in the rotating frame (right).

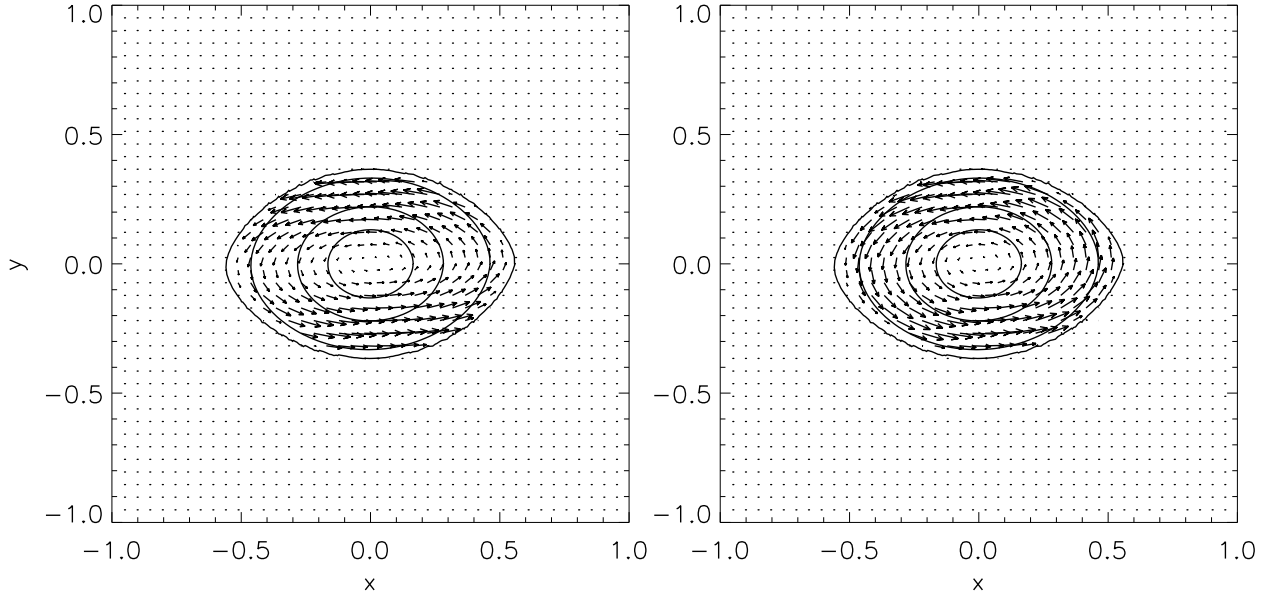


Fig. 6.— The same as Fig. 5 but for the adjoint configuration. This $n = 1$ model has $\omega = -0.201$ and $\lambda = -0.7433$, which corresponds to $\zeta = 1.70$. So the ellipsoidal configuration is spinning retrograde (clockwise) in the inertial frame, but the fluid is moving prograde (counterclockwise) rapidly in the rotating frame.

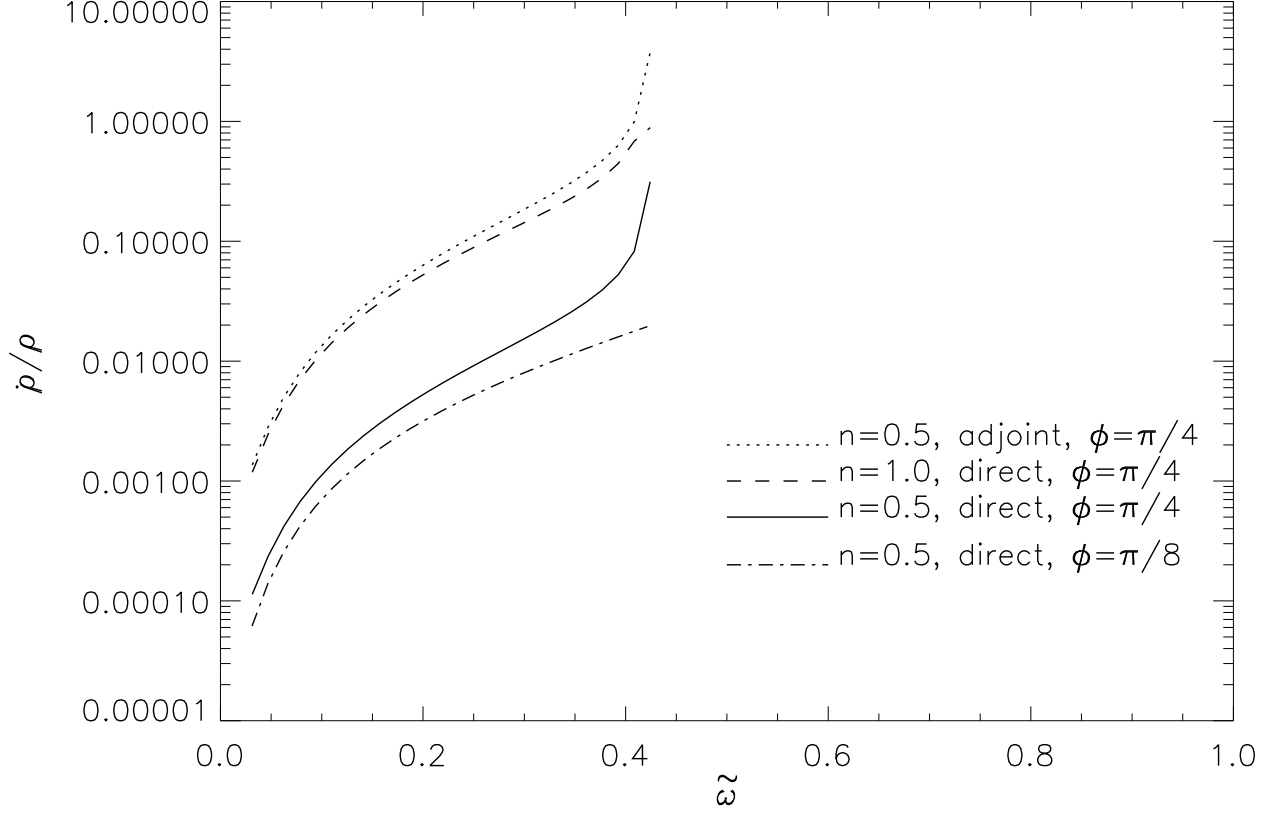


Fig. 7.— $|\dot{\rho}|/\rho$ is plotted in the equatorial plane as a function of cylindrical radius ϖ at angles $\phi = \pi/4$ and $\phi = \pi/8$ for the models shown in Figs. 3, 4, and 5. $|\dot{\rho}|/\rho$ is small in the interior of each model, but can become quite large near the outer edge where ρ approaches zero. Also, $|\dot{\rho}|/\rho$ is smaller for the models with the stiffer equation of state and for direct configurations.

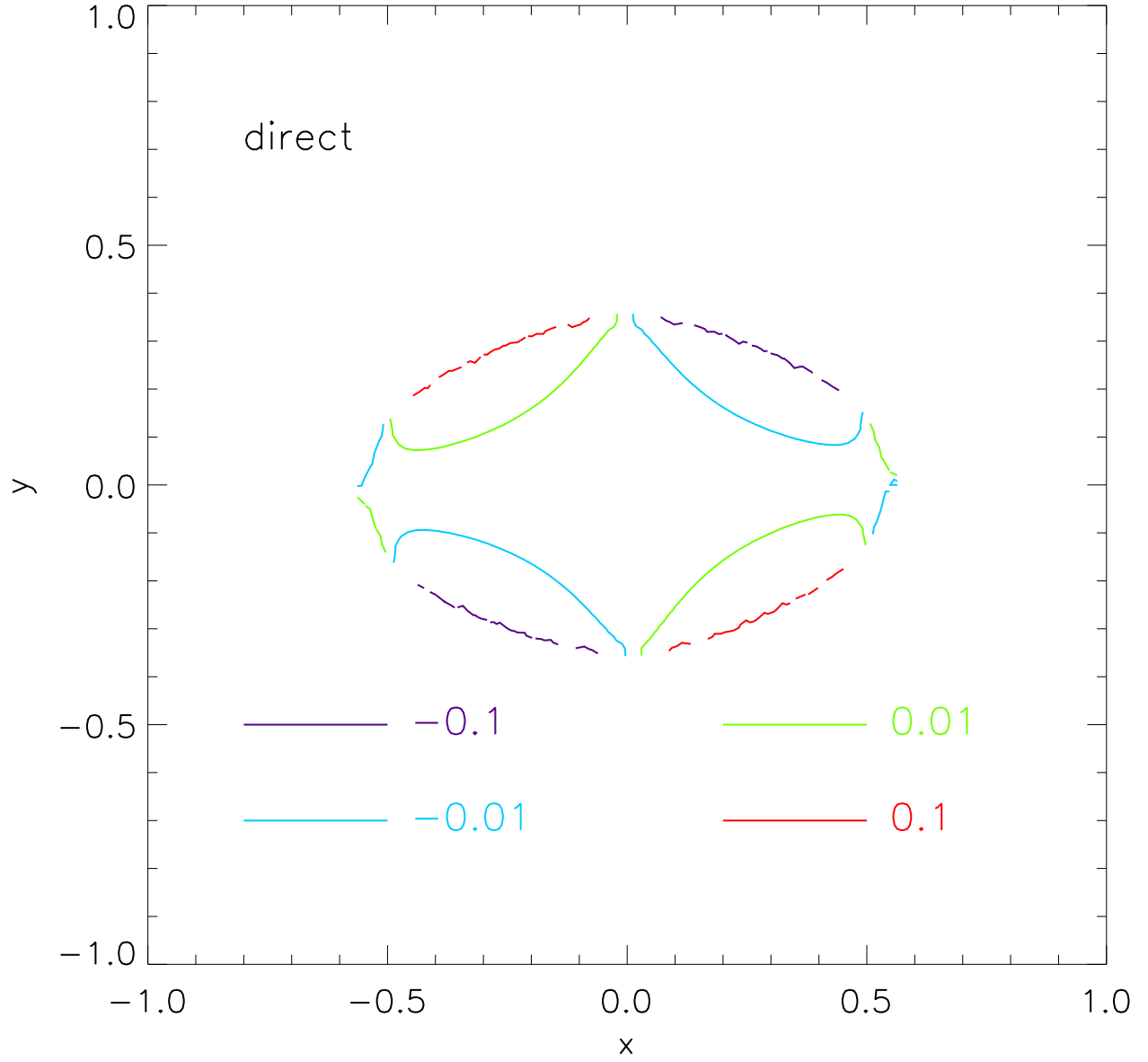


Fig. 8.— Contour map of $\nabla \cdot (\rho \vec{v})/\rho$ is plotted in the equatorial plane for the direct model shown in Fig. 3.

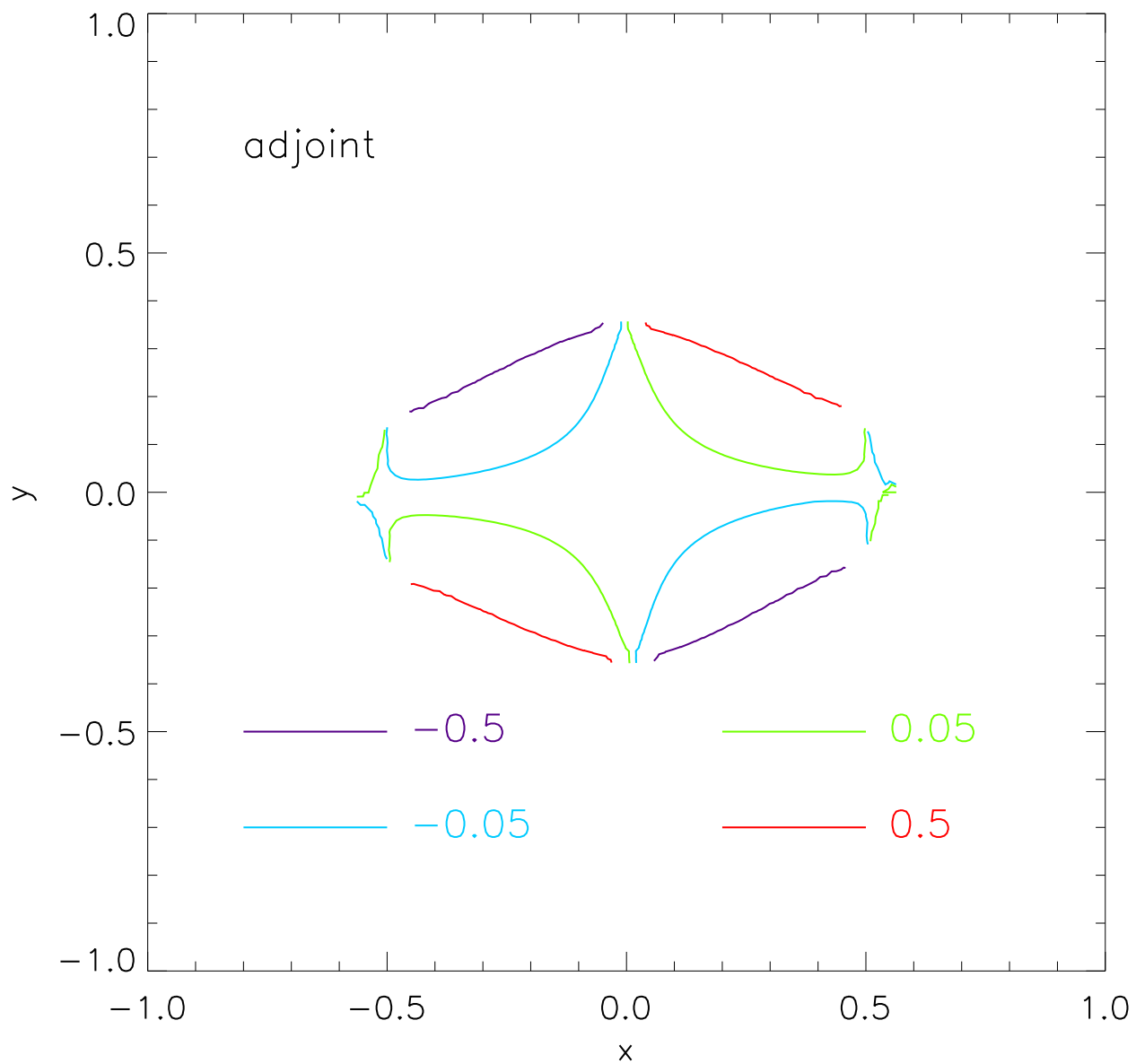


Fig. 9.— Contour map of $\nabla \cdot (\rho \vec{v})/\rho$ is plotted in the equatorial plane for the adjoint model shown in Fig. 4.

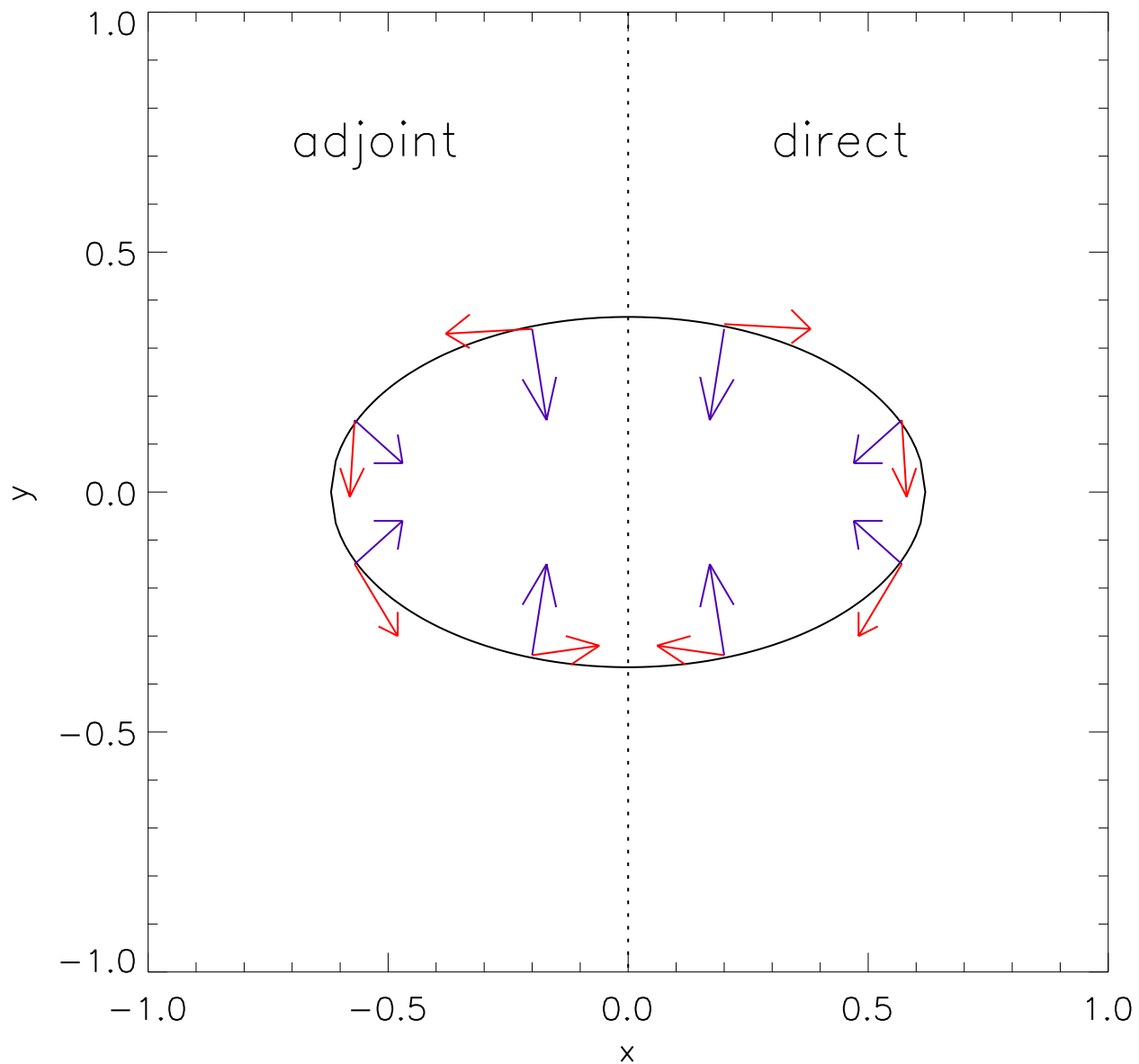


Fig. 10.— A combined schematic drawing of the density gradient (purple vectors) and velocity vectors (red) in the rotating frame for the direct (right panel) and adjoint (left panel) configurations shown in Fig. 3 and 4. The black ellipse denotes the surface of the ellipsoidal model. Notice that the fluid is moving prograde (retrograde) in the rotating frame for the chosen direct (adjoint) configuration.